Full Length Article

# Mechano-driven regeneration predicts response variations in large animal model based on scaffold implantation site and individual mechano-sensitivity

Gabriele Nasello [a,b], Antoine Vautrin [c], Jonathan Pitocchi [a,b,d], Mariska Wesseling [d], Jan Herman Kuiper [e,f], María Ángeles Pérez [a], José Manuel García-Aznar [a,*]

[a] *Multiscale in Mechanical and Biological Engineering, Instituto de Investigación en Ingeniería de Aragón (I3A), Instituto de Investigación Sanitaria Aragón (IIS Aragón), University of Zaragoza, Zaragoza, Spain*
[b] *Biomechanics Section, KU Leuven, Leuven, Belgium*
[c] *Ecole Nationale d'Ingénieurs de Metz, University of Lorraine, Metz, France*
[d] *Materialise NV, Leuven, Belgium*
[e] *Institute for Science and Technology in Medicine, Keele University, Keele, UK*
[f] *The Robert Jones and Agnes Hunt Orthopaedic Hospital, NHS Foundation Trust, Oswestry, UK*

## ARTICLE INFO

## ABSTRACT

It is well founded that the mechanical environment may regulate bone regeneration in orthopedic applications. The purpose of this study is to investigate the mechanical contributions of the scaffold and the host to bone regeneration, in terms of subject specificity, implantation site and sensitivity to the mechanical environment. Using a computational approach to model mechano-driven regeneration, bone ingrowth in porous titanium scaffolds was simulated in the distal femur and proximal tibia of three goats and compared to experimental results. The results showed that bone ingrowth shifted from a homogeneous distribution pattern, when scaffolds were in contact with trabecular bone (max local ingrowth 12.47%), to a localized bone ingrowth when scaffolds were implanted in a diaphyseal location (max local ingrowth 20.64%). The bone formation dynamics revealed an apposition rate of $0.37 \pm 0.28\%$/day in the first three weeks after implantation, followed by limited increase in bone ingrowth until the end of the experiment (12 weeks). According to *in vivo* data, we identified one animal whose sensitivity to mechanical stimulation was higher than the other two. Moreover, we found that the stimulus initiating bone formation was consistently higher in the femur than in the tibia for all the individuals. Overall, the dependence of the osteogenic response on the host biomechanics means that, from a mechanical perspective, the regenerative potential depends on both the scaffold and the host environment. Therefore, this work provides insights on how the mechanical conditions of both the recipient and the scaffold contribute to meet patient and location-specific characteristics.

## 1. Introduction

Despite the intrinsic healing capacities of bone tissue, revision arthroplasty caused by extensive bone loss and implant mechanical loosening is a major clinical burden [1]. The demand for total hip and knee arthroplasties is projected to reach 4 million procedures per year in the U.S. only for 2030 [2]. Improving implant longevity is therefore important to reduce the number of revision procedures and limit the cost for healthcare systems. The next generation of orthopedic implants aims to guide the bone healing process and inspires innovative solutions in the field of orthopedic regenerative medicine. In the short term, these solutions are mainly aimed at increasing the implant lifespan by improving biological fixation, while in the long term they are aimed at providing temporary implants that will degrade and be fully replaced by functional host tissue [3].

Porous metallic biomaterials, fabricated *via* additive manufacturing (AM), were recently proposed to address the lack of osteointegration in orthopedic implants [4,5]. With AM, orthopedic implants are fabricated with porous surfaces at the bone-implant interface, acting as scaffolds that enhance the biological engraft of the implant with the surrounding bone tissue [6–8]. Not only does a AM-fabricated implant fit the macro-scale geometries of individual applications, but it can also boost a regenerative response from the host [9–11]. In order to achieve functional integration with the host tissue, the optimization of 3D printed bone substitutes relies on, among others, the control of their mechanical properties to bear the weight of patients and the daily load-

ing the bone is subjected to [4]. A fine tuning of the apparent stiffness is appropriate for encouraging bone ingrowth into porous materials, given the intrinsic relationship between mechanical stimulation and bone adaptation [12]. AM is commonly associated to the development of porous scaffolds matching the local bone stiffness [13,14], although matching bone mechanical properties leaves out relevant aspects of the relation between mechanical stimulus and bone formation.

Firstly, the host sensitivity to mechanical stimulation has a critical impact on bone regeneration. The impact can be severe, such that weak responders, those with limited regenerative potential, may require permanent scaffolds for load-bearing applications [15]. A possible reason is the drastic alteration of the mechano-regulated processes of bone formation and resorption that takes place with aging [16,17]. As a consequence, the design of porous substitutes should take into account the variability in the host response. Secondly, the cellular response is site-specific and within a single subject may therefore vary from bone to bone and within the same bone. Indeed, the different parts of the skeleton experience mechanical stimulations that vary in intensity and type, causing specific adaptations by bone cells. Moreover, multiple biomechanical requirements are associated with specific histomorphometrical indicators and load transfer behaviors within the same bone. This is clearly visible in the differences in shape and proportions of trabecular bone of a single structure, such as in the femoral neck [18] and the fibula [19]. Depending on the local history of mechanical loading, it has been proposed that bone cells accommodate and respond differently to the same mechanical stimulation [20]. Thus, a macroscopic mechanical analysis of the performance of a bone substitute design needs to consider the dependence on the local biomechanical demand. It is well established thereby that control over the mechanical requirements of additively manufactured bone scaffolds can be potentially addressed with *in silico* modeling. By testing the efficacy of topological designs for each specific use and patient, computational algorithms are the most adequate approach to inspect the mechanobiological potential of 3D printed scaffolds [21,22]. An optimization framework implementing the FE method already verified that the local stiffness of mechanobiologically optimized titanium (Ti) scaffolds enhances endogenous bone regeneration, but did not consider how the formation of novel bone tissue alters the mechanical environment [23].

The implementation of phenomenological models *in silico* describes the influence of mechanical forces on the adaptation or the regeneration of bone tissue [24,25]. The simulation of bone mechano-regulation or regeneration processes can model their dynamics, in terms of continuous variation of bone mechanical properties [21,26]. When applied to porous scaffolds, regeneration algorithms elucidated the relationship between the tissue being formed within the pores and the loading environment, as well as the mechanical benefits of a degrading scaffold during bone formation [27,28]. However, no previous model of mechano-driven bone ingrowth has estimated the effect of local biomechanical demand and individual response variability on scaffold regenerative performance. There is a need for a wider evaluation of the mechanical interplay between scaffold and host subject.

Following the need of modeling the scaffold regenerative potential for patient-specific applications, the purpose of this study is to evaluate the scaffold performance based on the biomechanical contributions of both the host and the scaffold itself. We hypothesized that (1) local mechanical stimuli determine the distribution of bone ingrowth inside a scaffold and that (2) inter and intra-animal variations require subject-specific parameters to describe the local biomechanical demand and individual sensitivity to mechanical stimulus. Therefore, we developed a computational model of mechano-driven bone regeneration in porous scaffolds where the local mechanical environment and the regenerative potential of an individual host regulate the bone ingrowth within the scaffold pores. Mechanical properties were constantly updated during each analysis and model parameters represented the host reaction. We

calibrated the model by means of *in vivo* animal data (goat) of bone ingrowth in 3D printed porous Ti scaffolds, where scaffolds were inserted in distinctive implantation sites and in different recipients. This computational model presents a subject-specific applicability on the evaluation of the scaffold regenerative potential. From a mechanical perspective, it evaluates the scaffold regenerative performance for each specific patient and in each implantation site.

## 2. Materials and methods

### 2.1. Mechano-driven bone regeneration model

#### 2.1.1. Mathematical formulation

Computational methods of mechano-regulation relate bone formation and/or resorption directly to a mechanical stimulus. We define bone formation as the process by which new bone tissue is formed by osteoblasts that differentiate from osteoprogenitor cells. When translated to macroscopic models where bone is a continuous material without a hierarchical structure, the mathematical formulation of bone mechano-regulation reduced to a relation between local strain levels and bone mineral density [27,29,30]. Here, we assumed that a simultaneous process of cell invasion and a bone formation phase regulated by the mechanical stimulus could simulate the bone regeneration process [31].

Cell invasion in the granulation domain (Fig. 1-A) was modeled as a diffusion process, where cell concentration $c$ in the scaffold pores was normalized to the maximum cell concentration (Fig. 1-B). It had a constant value of 1 at the bone-granulation interface and initial zero value in the scaffold pores [27].

From the mechanical perspective, the daily strain stimulus $\Psi$ was based on the effective tissue microstrain $\bar{\varepsilon}$, calculated from the strain energy density $W$ and the Young's modulus $E$ [32] (Fig. 1-B). Together with the daily strain history, the strain level described the importance of each load cycle in the mechanical stimulus [33].

Earlier studies have implemented relations between mechanical stimulus and bone remodeling [34] to predict tissue regeneration in bone scaffolds [27]. These studies imply that bone formation occurs for values of the mechanical stimulus above a reference value, which could be identified with the local stimulus $\Psi_{local}^*$ in the neighboring area [35]. In the present model, the mathematical formulation of the bone volume deposition rate $\dot{V}$ assumed that (1) bone formation is proportional to mechanical stimulus $\Psi$ up to a maximum bone deposition rate $\dot{V}_{max}$ [36], (2) no bone resorption took place for low $\Psi$ [31] and (3) bone formation initiated for mechanical stimuli higher than a fraction $\alpha$ of the local mechanical stimulus $\Psi_{local}^*$ (Fig. 1-C). $\Psi_{local}^*$ was calculated as the volume-averaged daily strain stimulus in the bone at the location where the scaffold was to be placed and the immediate surrounding area, thus covering the implant region and also the peri-implant region that is mechanically altered after insertion of the implant [37]. The linear relationship between bone formation and mechanical stimulus was represented by subject-specific constant of bone volume deposition rate $k$. This constant was assumed to represent the capacity for mechanosensation of the single organism, thus it was a patient-specific parameter. On the other hand, the biomechanical demand was considered to be location-based, thus $\Psi_{local}^*$ and $\alpha$ varied within the same organism for different implantation sites. The detailed mathematical description of the bone regeneration model is given in Supplementary Material - 1.

#### 2.1.2. Numerical implementation

The mathematical model of mechano-driven bone regeneration was solved with FE methods implemented in ABAQUS 6.14 (Dassault Systèmes, Suresnes, France). The concurrent events of mechanical regulation and cell invasion required a sequential solution and update during the FE analysis. The mechanical behavior of the system was simu-
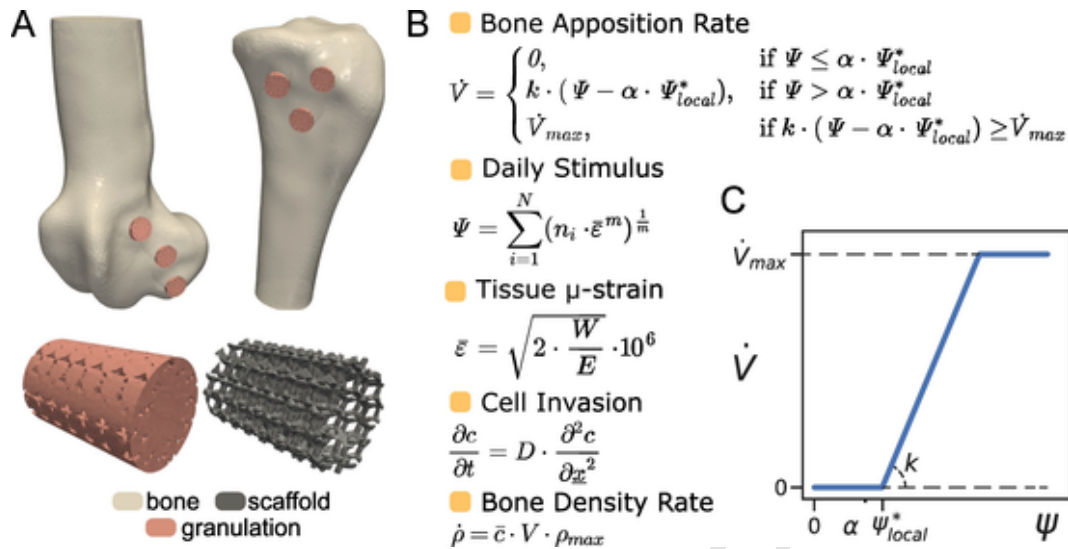
**Fig. 1.** Overview of the mechano-driven bone regeneration model. (A) Representative femoral and tibial *in silico* models of mechano-driven bone ingrowth and detail of a scaffold-granulation unit, where the granulation tissue filled the scaffold pores. The scaffold-granulation units were inserted in each bone based on the location extracted from CT image data. (B) Mathematical formulation of the mechano-driven model of bone ingrowth. The model consisted of a simultaneous process of cell invasion and a bone formation phase regulated by the mechanical stimulus (effective tissue microstrain), the daily load history and the mechanosensitivity of the host ($k$ constant). (C) Graphical display of the bone volume deposition rate proposed in the model. It was assumed that: bone formation is proportional to mechanical stimulus $\Psi$ up to a maximum bone deposition rate $\dot{V}_{max}$, no bone resorption took place for low $\Psi$ and bone formation initiated for mechanical stimuli higher than a fraction $\alpha$ of the local mechanical stimulus $\Psi_{local}^*$.

lated with a linear stress analysis, where the material properties of the newly formed bone were updated with a UMAT subroutine [38]. Cell invasion was simulated by means of a heat transfer problem, where temperature represented the non-dimensional cell concentration $c$ and was updated with a UMATHT subroutine. The use of a coupled thermal-stress analysis allowed the sequential implementation of the two processes, while the user subroutines continuously updated the bone formation process and the tissue mechanical properties (Supplementary Material - Fig. S1). To facilitate the model convergence in the first iterations, the initial time increment was set to 0.05 day. After, the software automatically increased the size of the subsequent increments up to 1 day.

### 2.2. Model application to an in vivo goat study

The experimental data used to calibrate the proposed model were taken from an unpublished animal study conducted by Materialise NV (Leuven, Belgium). Briefly, cylindrical porous titanium scaffolds were additively manufactured and three of them were inserted in each left femur and tibia of six goat models (Fig. 2-A,B). A regular porous structure ($\phi$ 8 mm, length 12 mm, porosity 71%) was built up of dodecahe-
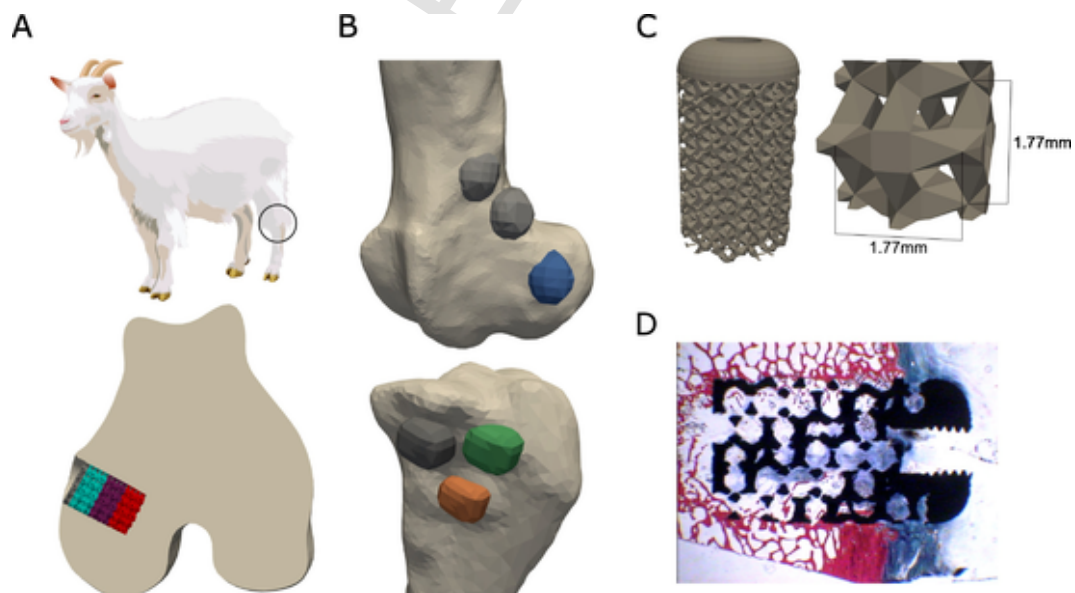


**Fig. 2.** Overview of the *in vivo* goat study. (A) Detail of the insertion of a 3D printed titanium scaffold in the epiphyseal location of a goat femur. Bone ingrowth was quantified with micro-CT imaging in the medullary (red), middle (purple) and periosteal (light blue) subregions of the scaffold. (B) Representative femur and tibia showing the locations where the titanium scaffolds were implanted within the bone. Bone ingrowth was assessed only for two scaffolds (blue, green) in epiphyseal and one (orange) in diaphyseal location. (C) Design of the cylindrical porous titanium scaffold fabricated by additive manufacturing as repetition of a dodecahedron unit cell with thick struts (shown in the detail). (D) Histological analysis confirmed the novel formation of bone tissue within the scaffold pores after 12 weeks from surgery. Samples were stained with Stevenel's blue (connective tissues) and Van Gieson's picro-fuchsin (staining bone in red). (For interpretation of the references to color in this figure legend, the reader is referred to the web version of this article.)

dron unit cell with thick struts (strut thickness 0.50 mm and mean pore size 1.77 mm) and covered with a solid cap to facilitate press-fit insertion into the bone (Fig. 2-C). The apparent stiffness of the scaffold was 2 GPa (Materialise data). Empty scaffolds were implanted, not pre-seeded with cells or filled with bone graft. Three animals were euthanized at 6 weeks post-operatively, while the other three were euthanized at 12 weeks. CT scanning of the goats was performed only for those euthanized 12 weeks after implantation, thus computational models were based on their bone geometries (cases 1, 2 and 3 in Supplementary Material - Table S2). For each animal euthanized at week 6 and 12, four scaffolds were used to evaluate the shear strength of the bone-scaffold interface (pull-out test), while two scaffolds were imaged *ex-vivo* using microCT to quantify bone ingrowth (Supplementary Material - Table S2). Bone ingrowth was defined as the mineralized bone tissue detected by the microCT scans. MicroCT scans were performed on a Phoenix NanoTom S (GE Measurement and Control Solution, Wunstorf, Germany) at the Department of Materials Engineering of the KU Leuven (Leuven, Belgium). The scanner was equipped with a 180 kV/ 15 W high-performance nanofocus X-ray tube and a 2304 × 2304 pixel Hamamatsu detector. A tungsten target was used, and the applied voltage and current were 90 kV and 240 A, respectively. A 0.3 mm cupper filter was installed. Beam hardening correction was applied during reconstruction of the cross-sectional images with Phoenix Datos|x 2.0 reconstruction software (GE Measurement and Control Solutions). The reconstructed micro-CT dataset had an isotropic voxel size of 6.0 m. Later, a multi-level Otsu segmentation distinguished between the scaffold, bone and non-mineralized tissue [39]. Finally, bone tissue formation within the scaffold pores was studied by histological analysis and Van Gieson's picro-fuchsin staining (Fig. 2-D).

Overall, bone ingrowth after 12 weeks was assessed for the scaffolds inserted in the femoral condyle of all three goats, thus in contact with trabecular bone (Fig. 2-B). As for the tibiae, the scaffold in contact with more cortical bone was analyzed in two goats. For the remaining goat, bone ingrowth was quantified in a scaffold inserted in the tibial epiphysis (Fig. 2-B).

### 2.3. Implementation of the FE model

A FE model was built for modeling the *in vivo* goat study, simulating the femurs and the tibiae of the three goats euthanized at 12 weeks post-operatively. The FE model simplified host reaction immediately after scaffold implantation [40] by filling scaffold pores with granulation tissue, thus creating a "scaffold-granulation units". These scaffold-granulation units were inserted in the tibia or in the femur at the specific locations extracted from CT images (Fig. 2-B). The scaffold-granulation units consisted of the titanium scaffolds and the granulation tissue.

#### 2.3.1. FE discretization and material properties

All parts were computationally modeled with linear unstructured meshes (4-node tetrahedral elements, C3D4 for bone and scaffold, C3D4T for granulation) generated using automatic algorithms (Materialise 3-matic™ 14.0, Materialise, Leuven, Belgium). The scaffold-granulation unit was meshed once and later inserted in the femur or in the tibia for each simulated case.

*2.3.1.1. Femur and tibia* Firstly, CT images were segmented with a livewire technique (Materialise Mimics™ 22.0, Materialise, Leuven, Belgium) to extract the femur and the tibia geometries. Each bone model was trimmed 10 cm from the condyles and meshed with target edge length of 1.4 mm, resulting in approximately 400.000 elements. Hounsfield units (HU) from CT images were mapped onto the FE models [41] and a custom algorithm was developed in the Python programming language to adjust for the partial volume effect at the edge between cortical bone and soft tissue. The algorithm redefined the HU at any node of the bone surface to the one of the nearest internal node,

only if the inner HU value was higher than the outer [42]. After transforming HU into apparent density [43], bone material properties were assigned based on a continuous relationship between apparent density and Young's modulus for ovine bone taken from the literature [13] (Supplementary Material - Fig. S2). In the FE analysis, femur and tibia were modeled as a linear elastic material, where Young's modulus was determined from the density-modulus relationship and Poisson's ratio was set to 0.3 [43].

*2.3.1.2. Scaffold-granulation unit* The cylindrical titanium scaffold was uniformly meshed, with a maximum edge length of 0.55 mm. The porous domain within the scaffold was considered the granulation tissue of the model. Starting from a cylinder matching the titanium scaffold size, the granulation tissue domain was determined as a non-manifold assembly, with the titanium scaffold as intersecting entity. In this way, the two parts shared nodes and element surfaces at their interface. Each pair of nodes was constrained to have identical displacement (tie-constraint), ensuring matching scaffold and tissue displacements at their interface. After investigating three different mesh sizes, the granulation volume was meshed with a maximum edge length of 0.3 mm, so that the titanium-granulation unit constituted a cylindrical part of approximately 630.000 elements to subtract from the bone (Supplementary Material - Fig. S3). In the FE analysis, both the scaffold and the granulation tissue parts were modeled as linear elastic materials. For the titanium alloy, a Young's modulus of 104 GPa (Materialise data) and Poisson's ratio of 0.3 were used. For the granulation tissue, the mechanical properties followed the continuous relationship between apparent density and Young's modulus used for the femur and the tibia, with initial bone density $\rho_{initial}$ set to 0.001 $g/cm^3$, and Poisson's ratio set to 0.3.

#### 2.3.2. Boundary conditions

*2.3.2.1. Cell invasion* Cell invasion of the scaffold pores was implemented as a thermal diffusion process from the surrounding bone tissue, where the normalized cell concentration was maximum. Thus, the temperature of the surface nodes at the bone-granulation interface was set to 1 during the analysis. The bone-granulation interface comprised the cylindrical surface of the scaffold (Fig. 3-A) as well as the flat surface on the medullary side of the scaffold. Conversely, cell diffusion was obstructed from the flat surface on the periosteal side of the scaffold, where the scaffold had a solid cap used for the press-fit insertion.

*2.3.2.2. Mechanical loading* The anatomical landmarks of the hip, ankle and knee centers, as well as the centers of the condyles and the tibial plateaus, were identified in each femur and tibia [44]. Boundary and loading conditions were applied in a new co-ordinate system based on the femur [45] or the tibia [46] landmarks (Fig. 3-B,C). In the model, loads were applied to the condylar surfaces (Fig. 3-B), while boundary conditions were applied to both the trimmed diaphyses and the knee centers of the femur and tibia (Fig. 3-C). The application of displacement constraints at both ends of a long bone produces physiological deformation and minimizes reaction forces at the constrained nodes [47]. For this reason, displacements along the axial and the antero-posterior directions of a 5 mm radius area around the knee center were set to zero, similarly to the physiological boundary conditions applied in a previous femur model [47]. Moreover, displacements were fully constrained to zero in four nodes of the trimmed surfaces, while all other nodes of the trimmed surface had only their axial displacement constrained to zero (Fig. 3-C). In this way, all absolute displacements throughout the model were below 1 mm (Supplementary Material - Fig. S4).Contact forces were based on experimental studies in ovine models quantifying the total force at the knee joint during a gait cycle [48,49]. All forces were scaled to the animal body weights (Table 1). The distribution of the total knee contact force over the contact areas was based on the force distribution as determined by a validated musculoskeletal model of a human knee while squatting [50].
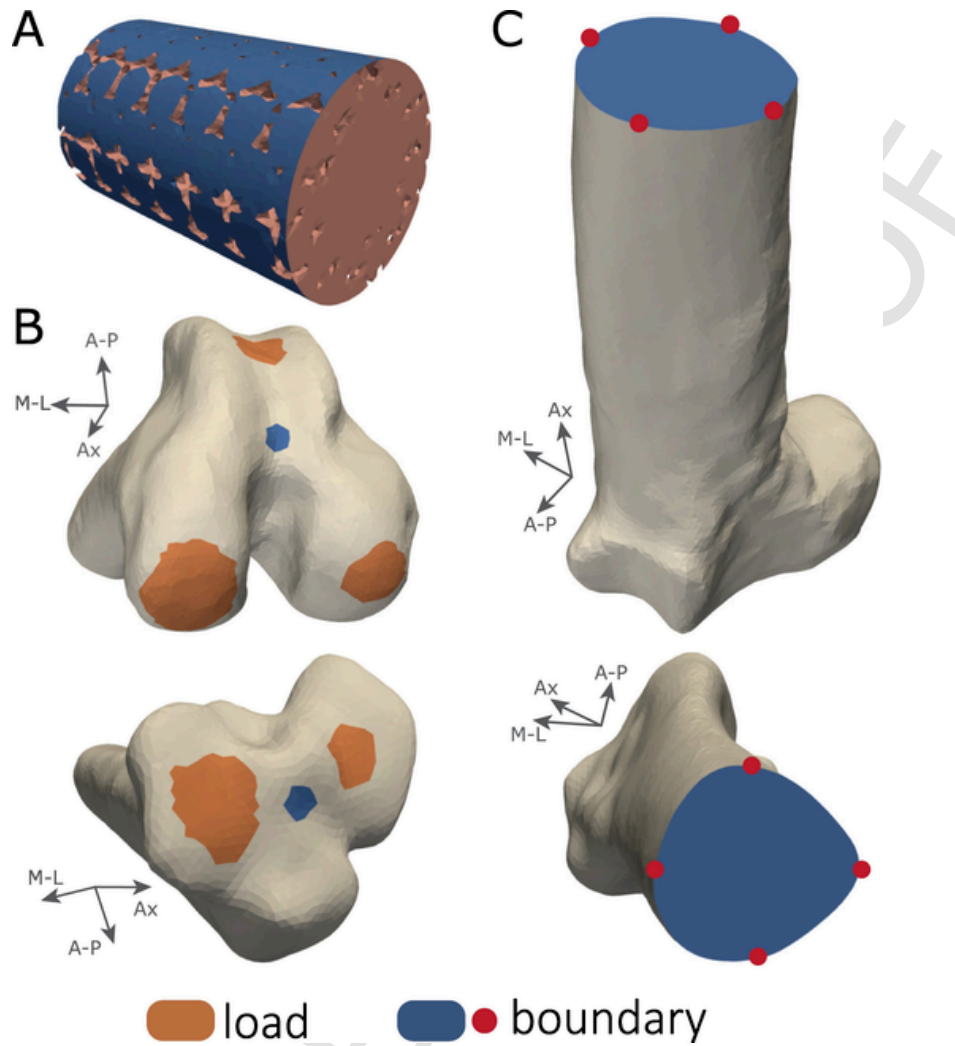
**Fig. 3.** Boundary and loading conditions of the finite element model of bone regeneration. Boundary conditions were applied to the blue surfaces, while loading conditions to the orange regions. (A) Granulation tissue. The boundary condition of the thermal diffusion analysis was applied at the granulation-bone interface, assuming a constant and maximum normalized cell concentration. (B) Loading and boundary conditions at the knee joint. The displacement of a 5 mm radius area around the knee center was set to zero along the antero-posterior (A-P) and the axial directions (Ax). The total forces are distributed over the contact areas of the patella and the condyles. (C) Boundary conditions on the distal femur and proximal tibia. (For interpretation of the references to color in this figure legend, the reader is referred to the web version of this article.)

**Table 1**
Summary of the loading conditions applied on the femur and the tibia. Knee joint forces were scaled to the body weight and distributed over the different contact areas of the femur and the tibia. Forces were distributed over the patella and the condyles for the femurs and over the tibial plateaus for the tibiae. All forces were applied along the axial, the antero-posterior (A-P) and the medio-lateral (M-L) directions. Animal weights are expressed in kg, age is expressed as years at the beginning of the *in vivo* experiment, while all forces are in N.

| Femur | Age | Weight | Axial | Patella | | Medial condyle | | | Lateral condyle | | |
|---|---|---|---|---|---|---|---|---|---|---|---|
| | | | | A-P | M-L | Axial | A-P | M-L | Axial | A-P | M-L |
| Case 1 | 2.8 | 72 | 554 | −680 | 25 | 605 | 815 | 3 | 367 | 369 | −66 |
| Case 2 | 3.7 | 65 | 500 | −614 | 22 | 547 | 736 | 3 | 332 | 333 | −60 |
| Case 3 | 2.8 | 58.5 | 450 | −553 | 20 | 492 | 662 | 2 | 298 | 300 | −54 |

| Tibia | Age | Weight | MEDIAL PLATEAU | | | LATERAL PLATEAU | | |
|---|---|---|---|---|---|---|---|---|
| | | | Axial | A-P | M-L | Axial | A-P | M-L |
| Case 1 | 2.8 | 72 | −1009 | −91 | 73 | −511 | −118 | 14 |
| Case 2 | 3.7 | 65 | −911 | −82 | −66 | −461 | −107 | 13 |
| Case 3 | 2.8 | 58.5 | −820 | −74 | 59 | −415 | 96 | 12 |

According to the musculoskeletal model, forces were divided over the contact areas of the patella and the condyles, while in the tibia they were divided over the tibial plateaus (Table 1) [50]. Bone remodeling and regeneration algorithms commonly use peak loadings during walking to quantify mechanical stimulation [31,34,51], which corresponds to 60° of knee flexion in the ovine gait cycle [48]. Therefore, total knee joint forces were distributed based on the proportions between medial and lateral contact forces measured in the musculoskeletal model at the position of 60° of flexion [50].

### 2.4. Post-processing FE output

#### 2.4.1. Local daily strain stimulus

The local daily strain stimulus $\Psi_{local}^*$ was calculated first in the neighboring area of the bone scaffold. Before each remodeling analysis, the daily strain stimulus $\Psi$ was measured for all femur elements within a cylinder of 8 mm radius and 16 mm length centered on the scaffold-granulation unit. $\Psi_{local}^*$ was then computed as a weighted average, with the element volumes as weights.

#### 2.4.2. In silico microCT and bone ingrowth assessment

The computational model included all scaffolds implanted in each animal to properly account for each scaffold's effect on the local mechanical environment. However, only the numerical predictions of the microCT imaged scaffolds were analyzed and used to calibrate the computational model. In order to quantitatively compare numerical predictions with *in vivo* experimental measurements, the simulation outputs were processed similarly to *in vivo* data [13]. At the end of each analysis, an Otsu thresholding algorithm separated the non-mineralized tissue from the newly formed bone in the granulation tissue. The identification of a medullary, middle and periosteal subregion within the granulation tissue (length 3.5 mm each) led to the bone ingrowth assessment, as performed in the *in vivo* procedure. The periosteal subregion was the closest to the external surface of the bone, while the medullary subregion was the furthest (Fig. 2).

### 2.5. Parameter estimation

The constant of bone volume deposition rate $k$ and the reduction factor $\alpha$, introduced in the mathematical model of bone regeneration, are directly associated with physiological quantities. They represent the mechano-sensitivity of the organism and the reduction of the reference stimulus initiating bone formation in the peri-implant region, respectively. Therefore, model calibration comprised identifying a subject-specific $k$ and a location-specific $\alpha$ that minimized the difference between computational and *in vivo* experimental results. The factor $\alpha$ was investigated in the range (1, 100) [%], since it was a reducing factor of the local reference strain stimulus. The constant $k$ was investigated in the range $(1 \cdot 10^{-5}, 9 \cdot 10^{-4})$ [% · µstrains$^{-1}$ · day$^{-1}$], which included the values of similar parameters used for bone regeneration [27] and remodeling [54] models (Supplementary Material - Table S3). When calibrating the model, the residual sum of squares (RSS) were first calculated for all numerical outcomes. Since $\alpha$ was a location-specific parameter, we determined the values of $\alpha$ that minimized the RSS for each value of $k$. Next, samples were grouped by recipient and we determined the value of $k$ that minimized the RSS for the whole recipient. Therefore, both $\alpha$ and $k$ were determined by minimizing of the RSS. On the one hand, the determination of $\alpha$ allowed intra-subject variation. On the other hand, the determination of $k$ required that it was the same for samples within the same subject.

The diffusion constant $D$ indicates the migration at which the host cells invade the granulation domain. Given that $D$ represented the whole cell population, the mechano-driven model of bone regeneration was calibrated with $D$ set to 0.01 mm$^2$/day, representing the midpoint of the range of diffusion constants used in a previous bioregulatory model of bone healing [52]. By way of sensitivity analysis, the computation was then repeated with $D$ set to 0.1 and 0.001 mm$^2$/day. Table 2 shows the remaining model parameters used in the FE analysis.

### 2.6. Temporal evolution of bone ingrowth

Bone ingrowth predictions were computed at each time increment of the numerical analysis and the temporal evolution was defined for the whole period simulated (12 weeks). As for the *in vivo* data, bone ingrowth was assessed for samples located in the femoral epiphysis of all goats, while in the tibiae two scaffold were in contact with compact bone and another one was in contact with trabecular bone (2-B,C). In the *in vivo* data, bone ingrowth was quantified in both groups euthanized at different timepoints (6 and 12 weeks). Numerical predictions were computed for the experimental group euthanized at week 12, and the temporal evolution of the bone ingrowth was compared to experimental data at 6 and 12 weeks.

### 2.7. Statistics

The Python programming language was used to run all the statistical analyses. We used repeated measures correlation (rmcorr) to compare numerical predictions of bone ingrowth in each subregion to the experimental data, since the assumption of error independence between observations was violated for predictions within the same recipient [55]. The repeated measures correlation coefficient $r_{rm}$ and its 95% confidence interval (CI) were used as measure of goodness of fit of the computational model.

## 3. Results

### 3.1. In vivo bone ingrowth in distal femur and proximal tibia

After 12 weeks from surgery, bone formation mostly occurred in the outer pores of the scaffold for all samples, with limited ingrowth in the core (Fig. 4) and different distribution depending on the anatomical location. When implanted *in vivo*, scaffolds in contact with trabecular bone (Fig. 5, green and blue scaffolds) had a homogeneous bone ingrowth distribution throughout the medullary, the middle and the periosteal subregions. Conversely, close to the tibial diaphysis bone ingrowth was substantially shifted in the periosteal subregion (Fig. 5, orange scaffolds). Moreover, a single animal (case 1) had both the highest periosteal bone ingrowth for the scaffold in contact with compact bone and the highest mean bone ingrowth for the scaffold in contact with trabecular bone (Fig. 5-B, left column). Bone ingrowth was also quantified in the femoral epiphysis for a different group of recipients euthanized 6 weeks after surgery. Bone ingrowths did not markedly differ at weeks 6 and 12 in any subregion (Fig. 6).

**Table 2**
Finite element parameters of the bone regeneration algorithm.

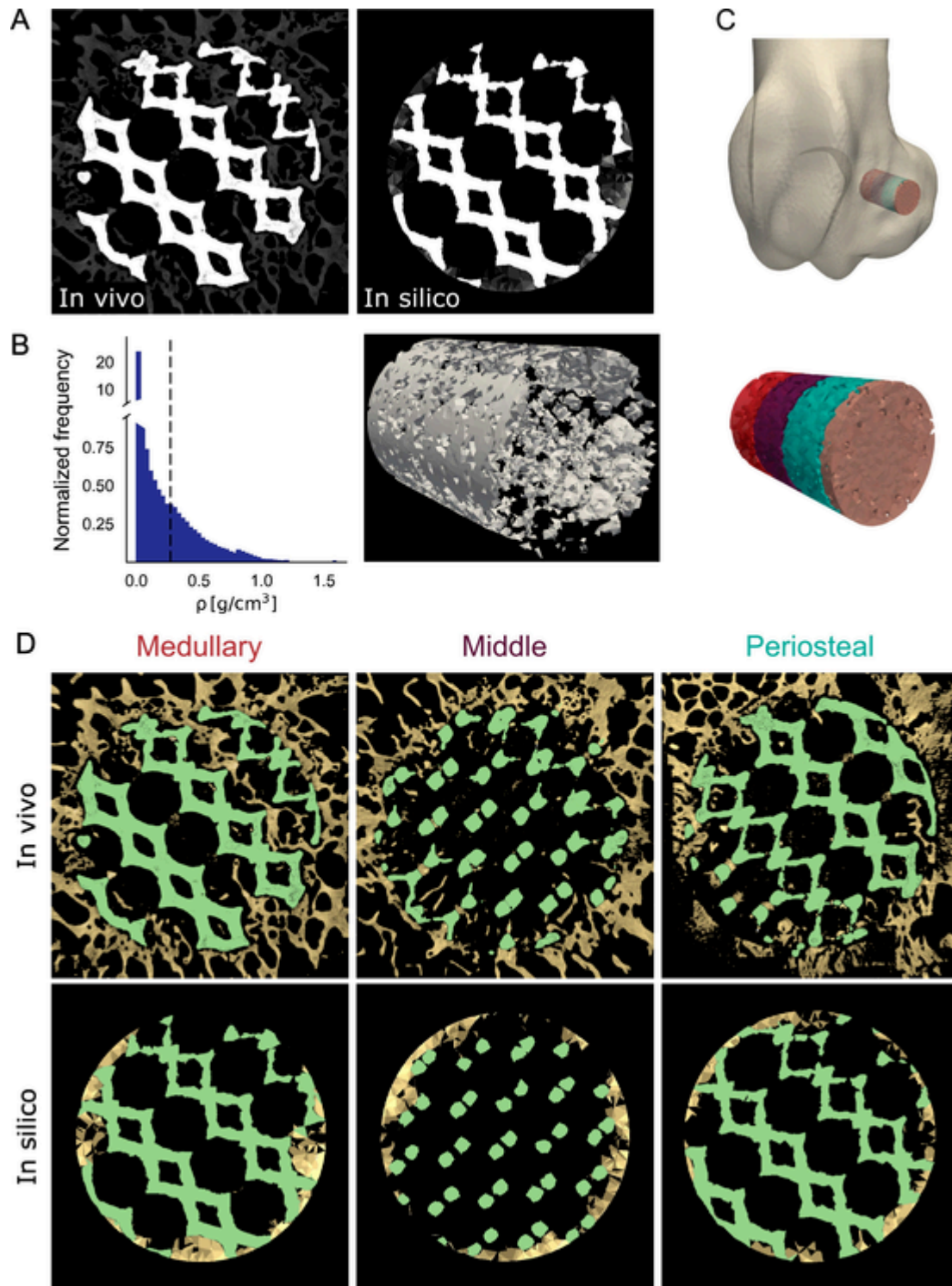| Parameter | Description | Value | Unit | Ref |
|---|---|---|---|---|
| $\rho_{initial}$ | Initial bone mineral density | 0.001 | $\frac{g}{cm^3}$ | – |
| $D$ | Diffusion constant | 0.01 | $\frac{mm^2}{day}$ | Range in [52] |
| $m$ | Daily strain history parameter | 4 | adim | [34] |
| $N$ | Number of loading cycles | 10,000 | $\frac{cycles}{day}$ | [53] |
| $\dot{V}_{max}$ | Maximum bone deposition rate | 4 | $\frac{\%}{day}$ | Adapted from [36] |
| $\rho_{max}$ | Maximum bone mineral density | 1.6 | $\frac{g}{cm^3}$ | [13] |

**Fig. 4.** *In silico* microCT. (A) Representative microCT image of bone forming within the defect located in the goat femoral epiphysis (case 1) at the end of the *in vivo* experiment (12 weeks) and *in silico* microCT image of the comparable location in the computational model of bone regeneration. (B) Left - Normalized count of elements in the granulation tissue of the *in silico* model at the end of the simulation. Dash line represents the Otsu's threshold used to separate the mineralized part of the granulation domain from the not-mineralized one. Right - *In silico* CT rendering of the bone ingrowth into the porous scaffold. (C) Location of the defect in the goat femoral epiphysis simulated in the *in silico* model and detail of the granulation domain (pink) with the medullary (red), middle (purple) and periosteal (light blue) subregions highlighted. (D) Representative *In vivo* and *in silico* microCT slices of the medullary, middle and periosteal subregions where bone is labeled in yellow and metal is labeled in green. (For interpretation of the references to color in this figure legend, the reader is referred to the web version of this article.)
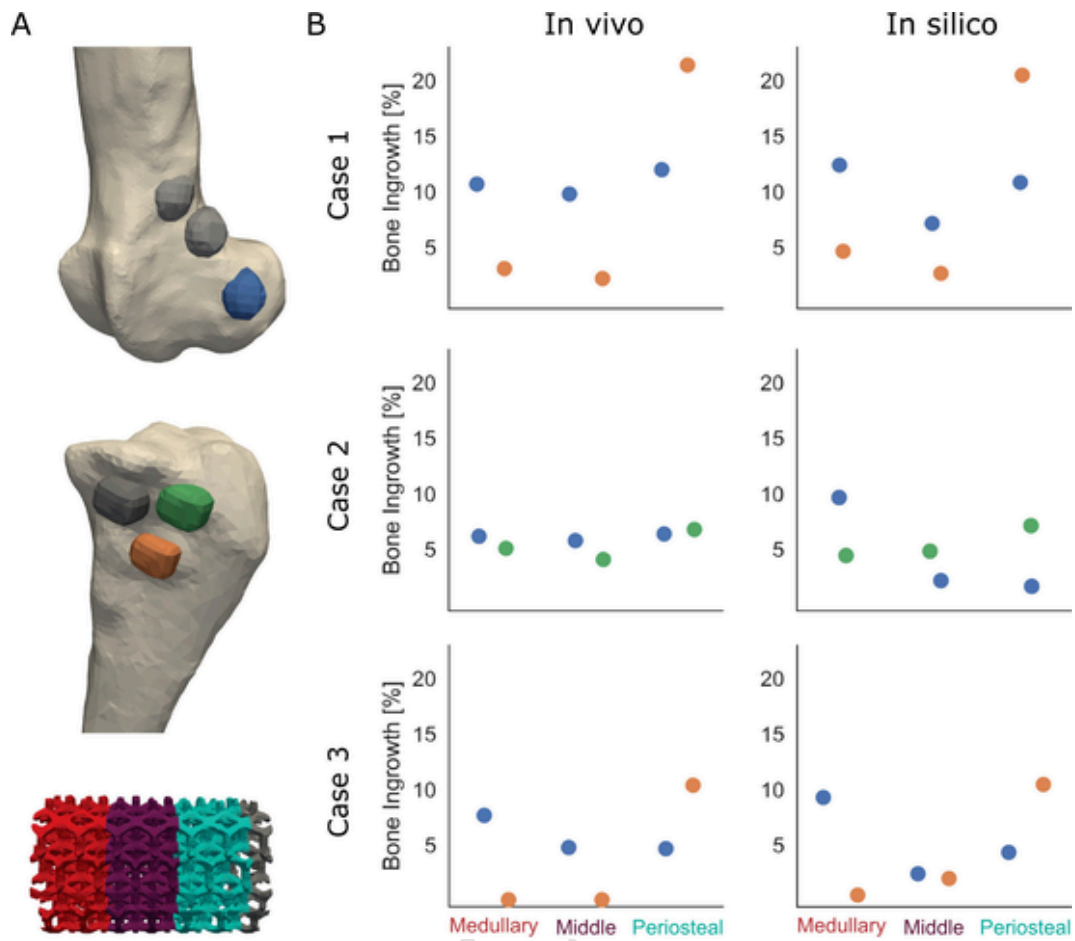
**Fig. 5.** Mechano-driven regeneration predicted bone ingrowth distribution in different scaffold locations. Bone ingrowth was assessed in six different scaffolds inserted into the left femurs and the tibiae of three different goats (cases) after 12 weeks from implantation. (A) Representative femur and tibia models showing the epiphyseal (blue, green) and diaphyseal (orange) locations of the titanium bone scaffolds. The scaffolds were individually simulated with the finite element model of mechano-driven bone regeneration. Three-dimensional view of the porous titanium scaffolds (gray) with the medullary (red), middle (purple) and periosteal (light blue) subregions highlighted. (B) Comparison of bone ingrowth quantification between *in vivo* and *in silico* models. (For interpretation of the references to color in this figure legend, the reader is referred to the web version of this article.)
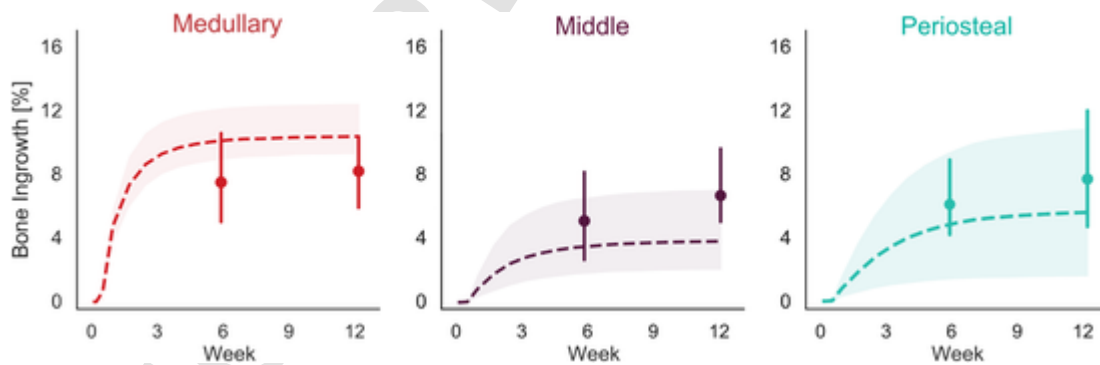


**Fig. 6.** The temporal evolution of bone ingrowth in porous titanium scaffolds revealed limited increase in bone ingrowth after 3 weeks from implantation. Temporal evolution of the bone ingrowth in the medullary, middle and periosteal regions of titanium porous scaffolds inserted in the femoral epiphysis of goat animal models. Comparison between *in silico* (dashes) and *in vivo* (points) results. Point plots and dashed lines denote the mean of $n = 3$ samples, with error bars and error bands representing 95% of confidence interval.

### 3.2. In silico microCT

Based on the normalized tissue density histogram at the end of the computational analysis, the Otsu's segmentation determined an optimal density threshold of $0.251 \pm 0.068$ g/cm$^3$ to separate two tissue types, leading to the identification of the newly formed bone in the scaffold pores (Fig. 4-B). In addition, the apparent density of the newly formed bone after the last iteration covered the ranges of both trabecular bone

($\rho < 0.8$ g/cm$^3$) and the one separating trabecular from cortical bone ($0.8 < \rho < 1.2$ g/cm$^3$) (Fig. 4-B). Similarly to the analysis of the *in vivo* data, medullary, middle and periosteal subregions were defined in the granulation tissue to assess bone ingrowth distribution (Fig. 4-C,D).

### 3.3. In silico predictions of bone ingrowth in distal femur and proximal tibia

The distribution of simulated mechano-driven bone ingrowth inside each scaffold correlated closely to the experimental data ($r_{rm} = 0.90$,

95% CI [0.72, 0.96], Supplementary Material - Fig. S5). Experimental and simulated ingrowth both showed a clear dependence on the anatomical location (Fig. 5-B), which corresponded to different distributions of the mechanical stimulus within the scaffold pores at implantation time (Supplementary Material - Fig. S6). Compared to experimental results, the model slightly overestimated the ingrowth in the medullary region for scaffolds in contact with trabecular bone (mean ingrowth $8.74 \pm 5.74\%$ *vs.* $7.43 \pm 3.87\%$, Fig. 5-B, green and blue scaffolds). Scaffolds inserted close to the diaphysis consistently showed higher bone ingrowth in the periosteal subregion when tuning the individual parameters $k$ and $\alpha$ (Supplementary Material - Fig. S7) and when changing the diffusion constant $D$ (Supplementary Material - Fig. S8).

The temporal evolution of predicted bone ingrowth highlighted a sharp increase in the first 3 weeks after implantation, during which the mean apposition rate for all scaffolds was $0.37 \pm 0.28\%$/day (Fig. 6). After that, bone ingrowth in all samples exhibited a plateau in all scaffold subregions, with a slight underestimation compared to the experimental data in the middle and periosteal subregions. At the end of the numerical analysis, bone ingrowth was mostly observed in the outer pores of the scaffolds, while it was limited in the scaffold core (Supplementary Material - Fig. S9).

### 3.4. Individual and local biomechanical demands

By fitting experimental results, the *in silico* model estimated a constant of bone volume deposition rate $k$ in the range of $[6,10]$ $10^{-5}$ %·strains$^{-1}$·day$^{-1}$, where the highest constant corresponded to the recipient reporting the highest bone ingrowths in both the femoral epiphysis and the tibial diaphysis (case 1, Fig. 7-B). Moreover, the local reference stimulus $\Psi_{local}^*$ ranged from 35 to 120 μstrains/kg, depending on the implantation site and the animal. It was consistently higher in the femur than in the tibia for all three cases simulated, with higher magnitudes corresponding to higher body weights (Fig. 7). As for the reduction factor $\alpha$, the model identified comparable values for different scaffold locations within each recipient. It ranged from 45% to 65% for both femoral and tibial locations of cases 2 and 3, while it was 20%

and 10% for the femoral and tibial location of case 1, respectively (Fig. 7-A). As a result, the mechanical stimulus triggering bone formation, which was the product of $\Psi_{local}^*$ and $\alpha$, had the opposite trend of the constant of bone ingrowth $k$: bone formation was triggered at lower values of mechanical stimulus in recipients with higher $k$ (Fig. 7-A).

## 4. Discussion

### 4.1. Mechano-driven regeneration predicts bone ingrowth distribution

The *in silico* model presented here revealed that a regenerative process purely based on mechanical stimulation predicts the bone ingrowth distributions, penetration depths as well as the bone formation dynamics observed *in vivo* when porous titanium bone scaffolds were implanted in different recipients and implantation sites. The model outcome indicated different mechanical states when the same scaffold architecture was implanted in the diaphyseal or in the epiphyseal location (Supplementary Material - Fig. S6).

Compared to *in vivo* data, medullary bone formation in the epiphyseal subregion was slightly higher whereas middle and periosteal bone formation in the same location were lower, which might be related to a wider surface in direct contact with bone tissue and aspirate bone marrow for the medullary subregion. The higher (but not significant) mean bone ingrowth was also observed *in vivo* both at 6 and 12 weeks in the medullary region (Fig. 6). Therefore, the computational model predicted both the *in vivo* trends of slightly higher bone ingrowth in the medullary subregion for the epiphyseal location and the significantly higher bone ingrowth in the periosteal subregion for the diaphyseal location.

The two different mechanical environments of the epiphyseal and diaphyseal implantation sites are the result of the adaptation of long bones. Indeed, on the one hand diaphysis adapted to bending and some torsional loadings [56]. On the other hand, the presence of cancellous bone confers epiphyses a shock absorbing function, homogeneously distributing their load throughout their volume [18].

Our results suggest that different biomechanical demands on the epiphyseal and the diaphyseal locations of a long bone induce distinc-
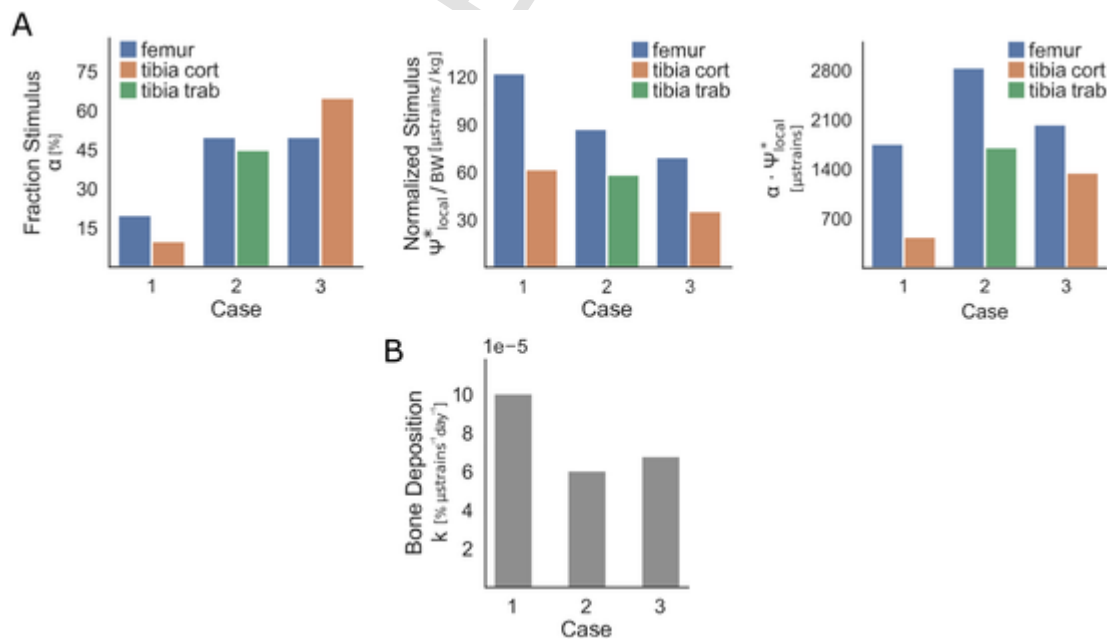


**Fig. 7.** Individual model parameters identified a stronger responder to mechanical stimulation and a mechanical stimulus initiating bone formation that varied among different implantation sites. Individual parameters of the mechano-driven model of bone regeneration applied to the three animal models studied. (A) Location-specific parameters. The local reference stimulus $\Psi_{local}^*$ was normalized by the body weight (BW) of each animal. Together with the reduction factor $\alpha$, they were location-dependent and denoted the biomechanical demand of the peri-implant environment, while the product $\alpha \cdot \Psi_{local}^*$ defined the mechanical stimulus triggering bone formation. (B) Subject-specific parameter. The constant of bone volume deposition $k$ denoted the subject's mechano-regulatory potential.

tive bone ingrowth distributions for the same scaffold microarchitecture. The use of the *in silico* approach revealed the regulatory role of the mechanical environment on the scaffold performance.

### 4.2. Mechanics limits complete bone formation within the scaffold pores

The use of an automatic algorithm to segment the bone tissue in the granulation domain resembled the common procedure applied with *in vivo* samples (Fig. 4). Bone density thresholds in the *in silico* results were around 0.25 g/cm$^3$, which is comparable to the lower range of apparent density in trabecular bone specimens [13]. By applying the same automatic thresholding technique, the computational model reached threshold values similar to the *in vivo* cases, strengthening the use of such mechano-regulatory theory to capture the dynamics of bone formation within the scaffold pores. Moreover, the mean bone volume deposition rate in the first three weeks after implantation was 0.37%/day, corresponding to a bone apposition rate of 3.7 μm/day for a bone surface of 1 mm$^2$. Such a bone apposition rate is comparable to the one of 1–2 μm/day observed in osteoids [57].

The analysis of the temporal evolution of bone ingrowth suggested that further deposition was not expected within the scaffolds pores. As bone started forming, the increase in the material properties led to a steady decrease of the mechanical stimulus, thus a reduction in the bone apposition rate. Mechanical stimulation in the scaffold core never reached the threshold value initiating bone formation, which suggests that the scaffold core was mechanically shielded by the newly forming bone in the outer pores. Thus, bone ingrowth was limited to the outer pores of the scaffold (Supplementary Material - Fig. S9). Once mechanical stimulation was also lower than the reference value in the outer pores, new bone tissue formation stopped entirely. *In silico* predictions estimated that the bone ingrowth plateau started 3 weeks after implantation, which might explain the similar values of *in vivo* bone ingrowth at 6 and 12 weeks (Fig. 6). Similarly, Chen et al. reported increasing mean bone ingrowth for porous titanium in ovine model up to 4 weeks. After 4 weeks, bone ingrowth did not increase until the last timepoint of the study (12 weeks) [58].

In general, the use of computational modeling in our study was essential for revealing information about the dynamic interaction between scaffold and host. Investigating the temporal evolution of bone ingrowth *in vivo* is expensive and has ethical concerns since it requires different animals for each timepoint, while the *in silico* model has no such concerns. Moreover, it provided a mechanical explanation of the limited bone penetration depth and the plateauing of bone ingrowth. Even though the model was only fit to results from the end of each experiment, it was still able to predict the limited bone ingrowth gain from the earlier timepoint.

### 4.3. Subject- and location-specific parameters model host mechano-response

Fitting experimental results is not only a successful strategy to calibrate an *in silico* model but, more importantly, it is decisive in extracting physiologically relevant information from the numerical analysis.

The parameter of bone volume deposition rate $k$ represents the host capacity to form novel bone tissue based on mechanical stimulation. In our model the identification of the optimal parameters for each simulation led to similar values of $k$ for cases 2 and 3, while a higher value of $k$ was found for case 1 (Fig. 7-B). Correspondingly, case 1 reported the highest absolute bone ingrowths in both the femur and the tibia (Fig. 5-B). The higher regenerative potential of this subject was captured by the *in silico* model, both in terms of total bone ingrowth and mechanosensitivity.

The model consistently showed higher local surrounding stimulus $\Psi_{local}^*$ for the femoral location in all cases studied, suggesting that the stimulus triggering bone ingrowth in the femur was higher compared to

the tibia. Bone adaptation to a local mechanical state might take into account that bone cells adapt to each characteristic state. Our results are consistent with the finding that instead of a single value throughout the skeleton, the minimum effective strain threshold is expected to vary locally depending on the loading environment, which defines the local biomechanical demand [20].

Best fits of the *in silico* model were obtained for values of the reduction factor of the reference stimulus $\alpha$ around 50% for cases 2 and 3, while its value was below 20% for case 1 (Fig. 5-B). From a biological perspective, the model suggested that bone formation within the scaffold pores was triggered by a fraction of the mechanical stimulus in the surrounding tissue. An earlier study combining *in vivo* experimental data with a finite element analysis of the local tissue mechanics, confirmed the alteration of the remodeling rules around a titanium implant. The authors reported bone started to form for mechanical stimuli 66% lower than those observed far from the implant [37].

Variability in the mechano-regulatory capacity of each subject depends on multiple factors, such as aging [17] or physical exercise [59]. More in general, the inherent variation between patients deeply affects the clinical outcome of regenerative products [60]. This source of variability is normally underestimated in preclinical models, where typically a small number of young, healthy animals are studied. The same issue arises with *in silico* models, which are commonly calibrated on single or ideal subjects [61].

Our study provides a mechanical interpretation of the response variability between individual recipients. By modeling the host mechanical response with a subject and a location specific parameter, we predicted bone formation within porous scaffolds and showed that the scaffold osteointegration cannot depend on its mechanical properties alone.

### 4.4. The mechanobiological potential of the host-scaffold unit

Taken together, our results indicate the essential role of host mechanical environment and mechano-sensitivity in the process of bone ingrowth into a porous bone scaffold.

Scaffolds with the same microarchitecture exhibited different bone ingrowth patterns when inserted in a diaphyseal or in epiphyseal location, which was associated with a diverse mechanical demand of the local environment. Interestingly, the *in silico* model facilitated determining a host-specific mechano-sensitivity, whose effects led to different bone ingrowth outcomes between recipients even though the scaffold was implanted at identical locations. The use of a mechano-based model also revealed specific aspects of the bone ingrowth dynamics, showing for instance that most of the increase in bone ingrowth occurred within the first 6 weeks after implantation. Similarly to the concept of the bone-healing unit, which produces a dynamic physiological response based on its biological and mechanical environment [62], the mechanical factor in the bone regeneration process depends on the dynamic interaction between the scaffold and the host mechanical environment, which combines the local tissue strain with anatomical location-dependent habitual strain levels and host-dependent strain sensitivity. Therefore, from a mechanical perspective, the combination of host and scaffold defines a mechanobiological unit contributing to the final scaffold regenerative potential.

Modeling the host response to the implantation of an additively manufactured porous material has direct implications on its design. Current patient-specific implants mainly aim to provide a tailored geometry and often include a porous metallic surface to improve their osteointegration, but they do not vary the mechanical properties of the porous surface depending on the specific implant location or the host regenerative potential. Scaffolds with lower apparent modulus enhance bone regeneration, although they must be stiff enough to ensure strength against mechanical failure [23]. Translated to the *in vivo* study analyzed, it is likely that a scaffold with a lower apparent modulus in

the core would have improved bone formation (Supplementary Fig. S9). In search of an optimal apparent modulus, degradable biomaterials or scaffolds with stiffness gradients are two potential approaches to reduce the scaffold apparent modulus and improve its mechanobiological performance. On the one hand, degradable scaffolds reduce mechanical properties over time [63], thus they gradually increase the strain throughout the scaffold pores. On the other hand, scaffold architecture can be finely tuned [64] to maximize both bone regeneration and scaffold stability, for example by designing lower apparent modulus where the bone tissue is likely to be formed while keeping the apparent modulus higher where bone formation is unlikely to happen. However, patients with lower response to mechanical stimulation might be insensitive to stiffness gradients and would probably need nondegradable scaffolds [15]. Therefore, a subject-specific model of mechano-driven bone regeneration could identify which patients benefit from a degradable scaffold or from a scaffold with a stiffness gradient or from a combination of both.

From a pragmatic perspective, the definition of the local biomechanical demand could rely on patient-specific models comprising bone mechanical properties, kinematic data and musculoskeletal load [65], while the clinical assessment of the individual mechano-sensitivity still requires further investigation. For example, the influence of the genome on bone mechano-responsiveness, already reported for inbred strains of mice [66], suggests that genetic diversity among patients might be associated to their individual mechano-sensitivity [67]. In addition, estrogen deficiency is another factor that impairs the bone cell mechano-sensation [68,69]. Therefore, mechano-sensitivity in computational models of mechano-driven bone regeneration might be correlated to the circulating estrogen levels, which are lower for female postmenopausal patients. Overall, the definition of a mechanobiologically-based approach, including individual estimates of the local biomechanical demand and mechano-sensitivity, would get closer to the specific needs of each recipient and facilitate endogenous bone formation.

### 4.5. Limitations

The use of FE methods is a well established procedure to define the bone mechanical state in different applications [70–72]. However, the mechano-driven model of bone regeneration used some assumptions that should be justified in line with the final conclusions here obtained.

Firstly, although the total forces applied on both the femurs and the tibiae were measured at the knee joint of ovine models, the distribution of mechanical loads over the femoral or tibial surfaces relied on a musculoskeletal model of a human knee while squatting. To the best of our knowledge, we do not know any study reporting the distribution of loading over the medial and lateral condyles in the knee joint for ovine animals during a gait analysis, and a model of the human knee was used because of its similarity to the ovine knee joint. Moreover, the present study considered mechanical loads proportional to the recipient body weight, while the loading history was assumed to be the same for all individuals. Nonetheless, activity levels following experimental interventions may vary between individuals [73]. Thus, future mechano-driven models of bone regeneration should include experimental *in vivo* studies tracking movement and activity for each subject.

Secondly, the regeneration model assumes that bone is the only tissue that could form within the scaffold pores. When micromotion occurs at the bone-scaffold interface, fibrous tissue could form and impair osteointegration [74]. However, at the start of the animal experiment, scaffolds were inserted through press-fitting, limiting micromotion at the bone-scaffold interface. Therefore, fibrous tissue formation was neglected in this study, although micromotion and eventual fibrous tissue formation should be modeled when the mechanical stability of the bone-scaffold interface is not guaranteed [75]. As for the properties of the newly formed bone tissue, the hierarchical structure of the tissue

was replaced by a homogeneous material with equivalent linear elastic properties [34]. In addition, the model assumed that fully developed bone tissue is formed after deposition [34]. As a result, the model did not include any analysis of the bone histomorphometry, although the efficacy of bone scaffolds is directly related to the quality of the newly formed bone. Differences in the apposition of mature lamellar bone have been recently reported for compliant and stiffer scaffolds, but variations in the final bone quality (*e.g.* woven-to-lamellar bone transition) corresponded to differences in the mechanical properties and final bone ingrowth [15]. Therefore, the model presented here cannot predict the histomorphometry of the regenerated bone tissue, but it can compare the global regenerative performance of different bone scaffolds for a patient-specific application, as well as the global performance of the same scaffold for different implantation sites.

Thirdly, the present model does not include the effect of precise bioregulatory factors on bone regeneration. Factors as the level of oxygen tension and angiogenesis can be more determinant to the osteogenic or chondrogenic differentiation of mesenchymal stem cells (MSCs) than mechanical stimulation [76]. In view of predicting progenitor cell fate, *in silico* models implementing bioregulatory factors have been extensively applied in the field of bone regeneration, with a strong focus on bone fracture healing processes [77,78]. However, the objective of our study was to isolate the mechanobiological problem of bone ingrowth into a porous scaffold and evaluate the influence of both the scaffold and the recipient. By reducing the cellular invasion process to a diffusion process coupled to mechano-driven regeneration, we defined a simplified system compared to the real conditions, but with the unique advantage of revealing the importance of mechanical stimuli in bone regeneration, which provided a biophysical interpretation of our results.

Furthermore, one additional limitation regards the *in vivo* data used to calibrate the model. The animal study was not designed to address the objectives of our work, thus relevant data that could strengthen the model calibration was never collected, such as CT scans of animals euthanized 6 weeks after surgery or a larger number of samples and locations where bone ingrowth was assessed. On the one hand, to demonstrate an absolute relationship between mechanical stimulus and bone ingrowth distribution, scaffolds should have been tested in the same implantation site while undergoing different loading conditions. On the other hand, only recent *in vivo* studies highlighted the importance of the local biomechanical demand and the individual response for bone regeneration [15], as well as the role of bone mechanobiology in the maximization of bone ingrowth. The different bone ingrowth patterns observed *in vivo* for the same scaffold architecture suggest that mechanics plays a key role in determining the final outcome, and the different magnitudes reported for each recipient support the hypothesis of inter-subject variability. Thus, we believe that our results call for new investigations on the *in vivo* impact of mechanobiologically-optimized scaffolds. Designing concomitant *in vivo* and *in silico* studies is the most successful strategy to maximize the clinical impact of such an optimization process.

### 5. Conclusions

Mechanical stimulus is intrinsically associated with the regenerative response to bone scaffolds in terms of bone formation. Successful application of a specific graft therefore requires a better understanding of the local mechanical microenvironment. The mechanical interaction between the scaffold and the subject relies on the local environment and the host response, in terms of both the distribution and the amount of newly formed bone within the scaffold. Using computational methods, we demonstrated that different implantation sites cause different mechanical conditions and induce distinctive patterns of bone ingrowth distribution, while the dynamics of mechanical stimulus limited bone penetration depth within the scaffold. The model calibration against *in*

*vivo* data revealed a stronger responder between the recipients as well as different mechanical stimuli initiating bone formation in the femur and in the tibia. The scaffold and the host defined a mechanobiological unit, whose dynamic state controlled the bone ingrowth process and the scaffold regeneration potential. From a clinical perspective, modeling the host mechanical response provides a mechanobiologically-based approach to meet both subject- and location-specific needs by tuning scaffold mechanical properties.

## Declaration of competing interest

The authors declare that the research was conducted in the absence of any commercial or financial relationships that could be construed as a potential conflict of interest.

## Acknowledgments

## Funding

## Data availability statement

The results reported in this paper were generated as part of the CuraBone project (Marie Skłodowska-Curie grant agreement No. 722535). Please contact the corresponding author for further information on data access policies. The Python modules developed to pre- and post-process ABAQUS simulations are available under https://github.com/gabnasello/fempygithub.com/gabnasello/fempy and https://github.com/gabnasello/odbhelpergithub.com/gabnasello/odbhelper.

## Appendix A. Supplementary data

Supplementary data to this article can be found online at https://doi.org/10.1016/j.bone.2020.115769.

## References

[1] K.J. Bozic, A.F. Kamath, K. Ong, E. Lau, S. Kurtz, V. Chan, T.P. Vail, H. Rubash, D.J. Berry, Comparative epidemiology of revision arthroplasty: failed THA poses greater clinical and economic burdens than failed TKA, Clin. Orthop. Relat. Res. 473 (6) (2015) 2131–2138, doi:10.1007/s11999-014-4078-8.

[2] S. Kurtz, K. Ong, E. Lau, F. Mowat, M. Halpern, Projections of primary and revision hip and knee arthroplasty in the United States from 2005 to 2030, The Journal of Bone & Joint Surgery 89 (4) (2007) 780–785, doi:10.2106/JBJS.F.00222.

[3] A.S. Brydone, D. Meek, S. Maclaine, Bone grafting, orthopaedic biomaterials, and the clinical need for bone engineering, Proc. Inst. Mech. Eng. H J. Eng. Med. 224 (12) (2010) 1329–1343 URL http://journals.sagepub.com/doi/10.1243/09544119JEIM770, doi:10.1243/09544119JEIM770.

[4] A.A. Zadpoor, Additively Manufactured Porous Metallic Biomaterials, 2019, doi:10.1039/c9tb00420c.

[5] L. Zhang, G. Yang, B.N. Johnson, X. Jia, Three-dimensional (3D) printed scaffold and material selection for bone repair, Acta Biomater. 84 (2019) 16–33, doi:10.1016/j.actbio.2018.11.039.

[6] J. Muth, M. Poggie, G. Kulesha, R. Michael Meneghini, Novel highly porous metal technology in artificial hip and knee replacement: processing methodologies and clinical applications, JOM 65 (2) (2013) 318–325 URL http://link.springer.com/10.1007/s11837-012-0528-5, doi:10.1007/s11837-012-0528-5.

[7] C.N. Kelly, J. Francovich, S. Julmi, D. Safranski, R.E. Guldberg, H.J. Maier, K. Gall, Fatigue behavior of As-built selective laser melted titanium scaffolds with sheet-based gyroid microarchitecture for bone tissue engineering, Acta Biomater. 94 (2019) 610–626, doi:10.1016/j.actbio.2019.05.046.

[8] A. Zadpoor, Design for additive bio-manufacturing: from patient-specific medical devices to rationally designed meta-biomaterials, Int. J. Mol. Sci. 18 (8) (2017) 1607, doi:10.3390/ijms18081607.

[9] X. Wang, S. Xu, S. Zhou, W. Xu, M. Leary, P. Choong, M. Qian, M. Brandt, Y.M. Xie, Topological design and additive manufacturing of porous metals for bone scaffolds and orthopaedic implants: a review, Biomaterials 83 (2016) 127–141, doi:10.1016/j.biomaterials.2016.01.012.

[10] S. Bose, S. Vahabzadeh, A. Bandyopadhyay, Bone tissue engineering using 3D printing, Mater. Today 16 (12) (2013) 496–504, doi:10.1016/j.mattod.2013.11.017.

[11] J. Henkel, M.A. Woodruff, D.R. Epari, R. Steck, V. Glatt, I.C. Dickinson, P.F.M. Choong, M.A. Schuetz, D.W. Hutmacher, Bone regeneration based on tissue engineering conceptions — a 21st century perspective, Bone Research 1 (3) (2013) 216–248, doi:10.4248/BR201303002.

[12] C. Turner, Three rules for bone adaptation to mechanical stimuli, Bone 23 (5) (1998) 399–407, doi:10.1016/S8756-3282(98)00118-5.

[13] S. Ghouse, N. Reznikov, O.R. Boughton, S. Babu, K.C. Ng, G. Blunn, J.P. Cobb, M.M. Stevens, J.R. Jeffers, The design and in vivo testing of a locally stiffness-matched porous scaffold, Appl. Mater. Today 15 (2019) 377–388, doi:10.1016/j.apmt.2019.02.017.

[14] X.-Y. Zhang, X.-C. Yan, G. Fang, M. Liu, Biomechanical influence of structural variation strategies on functionally graded scaffolds constructed with triply periodic minimal surface, Additive Manufacturing 32 (2020) 101015, doi:10.1016/j.addma.2019.101015.

[15] N. Reznikov, O.R. Boughton, S. Ghouse, A.E. Weston, L. Collinson, G.W. Blunn, J.R. Jeffers, J.P. Cobb, M.M. Stevens, Individual response variations in scaffold-guided bone regeneration are determined by independent strain- and injury-induced mechanisms, Biomaterials 194 (2019) 183–194, doi:10.1016/J.BIOMATERIALS.2018.11.026.

[16] A.I. Birkhold, H. Razi, G.N. Duda, R. Weinkamer, S. Checa, B.M. Willie, The influence of age on adaptive bone formation and bone resorption, Biomaterials 35 (34) (2014) 9290–9301, doi:10.1016/j.biomaterials.2014.07.051.

[17] H. Razi, A.I. Birkhold, R. Weinkamer, G.N. Duda, B.M. Willie, S. Checa, Aging leads to a dysregulation in mechanically driven bone formation and resorption, J. Bone Miner. Res. 30 (10) (2015) 1864–1873, doi:10.1002/jbmr.2528.

[18] E. Seeman, Bone quality: the material and structural basis of bone strength, J. Bone Miner. Metab. 26 (1) (2008) 1–8, doi:10.1007/s00774-007-0793-5.

[19] G.R. Cointry, L. Nocciolino, A. Ireland, N.M. Hall, A. Kriechbaumer, J.L. Ferretti, J. Rittweger, R.F. Capozza, Structural differences in cortical shell properties between upper and lower human fibula as described by pQCT serial scans. A biomechanical interpretation, Bone 90 (2016) 185–194, doi:10.1016/j.bone.2016.06.007.

[20] J.L. Schriefer, S.J. Warden, L.K. Saxon, A.G. Robling, C.H. Turner, Cellular accommodation and the response of bone to mechanical loading, J. Biomech. 38 (9) (2005) 1838–1845, doi:10.1016/j.jbiomech.2004.08.017.

[21] C. Metz, G.N. Duda, S. Checa, Towards multi-dynamic mechano-biological optimization of 3D-printed scaffolds to foster bone regeneration, Acta Biomater. 101 (2020) 117–127, doi:10.1016/j.actbio.2019.10.029.

[22] S. Giannitelli, D. Accoto, M. Trombetta, A. Rainer, Current trends in the design of scaffolds for computer-aided tissue engineering, Acta Biomater. 10 (2) (2014) 580–594, doi:10.1016/j.actbio.2013.10.024.

[23] A.-M. Pobloth, S. Checa, H. Razi, A. Petersen, J.C. Weaver, K. Schmidt-Bleek, M. Windolf, A.Á. Tatai, C.P. Roth, K.-D. Schaser, G.N. Duda, P. Schwabe, Mechanobiologically optimized 3D titanium-mesh scaffolds enhance bone regeneration in critical segmental defects in sheep, Science Translational Medicine 10 (423) (2018) eaam8828, doi:10.1126/scitranslmed.aam8828.

[24] J.M. García-Aznar, M.J. Gómez-Benito, M.Á. Pérez, M. Doblaré, Mechanobiological models for bone tissue. Applications to implant design, Biomechanics of Hard Tissues, Wiley-VCH Verlag GmbH & Co. KGaA, Weinheim, Germany, 2010, pp. 123–143, doi:10.1002/9783527632732.ch4.

[25] D.C. Betts, R. Müller, Mechanical regulation of bone regeneration: theories, models, and experiments, Frontiers in Endocrinology 5 (2014), doi:10.3389/fendo.2014.00211.

[26] L. Geris, J. Vander Sloten, H. Van Oosterwyck, Connecting biology and mechanics in fracture healing: an integrated mathematical modeling framework for the study of nonunions, Biomech. Model. Mechanobiol. 9 (6) (2010) 713–724, doi:10.1007/s10237-010-0208-8.

[27] J.A. Sanz-Herrera, J.M. García-Aznar, M. Doblaré, On scaffold designing for bone regeneration: a computational multiscale approach, Acta Biomater. 5 (1) (2009) 219–229, doi:10.1016/J.ACTBIO.2008.06.021.

[28] Y. Chen, S. Zhou, Q. Li, Microstructure design of biodegradable scaffold and its effect on tissue regeneration, Biomaterials 32 (22) (2011) 5003–5014, doi:10.1016/j.biomaterials.2011.03.064.

[29] S. Sturm, S. Zhou, Y.-W. Mai, Q. Li, On stiffness of scaffolds for bone tissue engineering—a numerical study, J. Biomech. 43 (9) (2010) 1738–1744 URL https://linkinghub.elsevier.com/retrieve/pii/S002192901000103X, doi:10.1016/j.jbiomech.2010.02.020.

[30] A. Carriero, A. Pereira, A. Wilson, S. Castagno, B. Javaheri, A. Pitsillides, M. Marenzana, S. Shefelbine, Spatial relationship between bone formation and mechanical stimulus within cortical bone: combining 3D fluorochrome mapping and poroelastic finite element modelling, Bone Reports 8 (2018) 72–80 URL https://linkinghub.elsevier.com/retrieve/pii/S2352187218300081, doi:10.1016/j.bonr.2018.02.003.

[31] J.A. Sanz-Herrera, J.M. García-Aznar, M. Doblaré, A mathematical model for bone tissue regeneration inside a specific type of scaffold, Biomech. Model. Mechanobiol. 7 (5) (2008) 355–366, doi:10.1007/s10237-007-0089-7.

[32] W. Pistoia, B. van Rietbergen, E.-M. Lochmüller, C. Lill, F. Eckstein, P. Rüegsegger, Estimation of distal radius failure load with micro-finite element analysis models based on three-dimensional peripheral quantitative computed tomography images, Bone 30 (6) (2002) 842–848, doi:10.1016/S8756-3282(02)00736-6.

[33] J.M. García-Aznar, T. Rueberg, M. Doblare, A bone remodelling model coupling microdamage growth and repair by 3D BMU-activity, Biomech. Model. Mechanobiol. 4 (2–3) (2005) 147–167, doi:10.1007/s10237-005-0067-x.

[34] D.R. Carter, G.S. Beaupré, Cancellous bone, Skeletal Function and Form, 13, Cambridge University Press, 2000, pp. 138–160, doi:10.1017/CBO9780511574993.007.

[35] T. Adachi, Y. Osako, M. Tanaka, M. Hojo, S.J. Hollister, Framework for optimal design of porous scaffold microstructure by computational simulation of bone regeneration, Biomaterials 27 (21) (2006) 3964–3972, doi:10.1016/j.biomaterials.2006.02.039.

[36] T. Adachi, Y. Kameo, M. Hojo, Trabecular bone remodelling simulation considering osteocytic response to fluid-induced shear stress, Philosophical Transactions. Series A, Mathematical, Physical, and Engineering Sciences 368 (1920) (2010) 2669–2682, doi:10.1098/rsta.2010.0073.

[37] Z. Li, D. Betts, G. Kuhn, M. Schirmer, R. Müller, D. Ruffoni, Mechanical regulation of bone formation and resorption around implants in a mouse model of osteopenic bone, J. R. Soc. Interface 16 (152) (2019) 20180667, doi:10.1098/rsif.2018.0667.

[38] ABAQUS/Standard User's Manual, Version 6.14, 2010.

[39] M. Sonnaert, G. Kerckhofs, I. Papantoniou, S. Van Vlierberghe, V. Boterberg, P. Dubruel, F.P. Luyten, J. Schrooten, L. Geris, Multifactorial optimization of contrast-enhanced nanofocus computed tomography for quantitative analysis of neo-tissue formation in tissue engineering constructs, PLoS One 10 (6) (2015) e0130227, doi:10.1371/journal.pone.0130227.

[40] J.M. Anderson, A. Rodriguez, D.T. Chang, Foreign body reaction to biomaterials, Semin. Immunol. 20 (2) (2008) 86–100, doi:10.1016/J.SMIM.2007.11.004.

[41] E.C. Pegg, H.S. Gill, An open source software tool to assign the material properties of bone for ABAQUS finite element simulations, J. Biomech. 49 (13) (2016) 3116–3121, doi:10.1016/j.jbiomech.2016.07.037.

[42] B. Helgason, F. Taddei, H. Pálsson, E. Schileo, L. Cristofolini, M. Viceconti, S. Brynjólfsson, A modified method for assigning material properties to FE models of bones, Med. Eng. Phys. 30 (4) (2008) 444–453, doi:10.1016/j.medengphy.2007.05.006.

[43] E. Schileo, E. Dall'Ara, F. Taddei, A. Malandrino, T. Schotkamp, M. Baleani, M. Viceconti, An accurate estimation of bone density improves the accuracy of subject-specific finite element models, J. Biomech. 41 (11) (2008) 2483–2491, doi:10.1016/j.jbiomech.2008.05.017.

[44] J. Victor, D. Van Doninck, L. Labey, B. Innocenti, P. Parizel, J. Bellemans, How precise can bony landmarks be determined on a CT scan of the knee?, Knee 16 (5) (2009) 358–365, doi:10.1016/j.knee.2009.01.001.

[45] J. Victor, D. Van Doninck, L. Labey, F. Van Glabbeek, P. Parizel, J. Bellemans, A common reference frame for describing rotation of the distal femur, The Journal of Bone and Joint Surgery. British volume 91–B (5) (2009) 683–690, doi:10.1302/0301-620X.91B5.21827.

[46] E.S. Grood, W.J. Suntay, A joint coordinate system for the clinical description of three-dimensional motions: application to the knee, J. Biomech. Eng. 105 (2) (1983) 136–144, doi:10.1115/1.3138397.

[47] A.D. Speirs, M.O. Heller, G.N. Duda, W.R. Taylor, Physiologically based boundary conditions in finite element modelling, J. Biomech. 40 (10) (2007) 2318–2323 URL https://linkinghub.elsevier.com/retrieve/pii/S0021929006004076, doi:10.1016/j.jbiomech.2006.10.038.

[48] G.N. Duda, K. Eckert-Hübner, R. Sokiranski, A. Kreutner, R. Miller, L. Claes, Analysis of inter-fragmentary movement as a function of musculoskeletal loading conditions in sheep, J. Biomech. 31 (3) (1997) 201–210, doi:10.1016/S0021-9290(97)00127-9.

[49] Z.F. Lerner, B.C. Gadomski, A.K. Ipson, K.K. Haussler, C.M. Puttlitz, R.C. Browning, Modulating tibiofemoral contact force in the sheep hind limb via treadmill walking: predictions from an opensim musculoskeletal model, J. Orthop. Res. 33 (8) (2015) 1128–1133, doi:10.1002/jor.22829.

[50] V. Vanheule, H.P. Delport, M.S. Andersen, L. Scheys, R. Wirix-Speetjens, I. Jonkers, J. Victor, J. Vander Sloten, Evaluation of predicted knee function for component malrotation in total knee arthroplasty, Med. Eng. Phys. 40 (2017) 56–64, doi:10.1016/j.medengphy.2016.12.001.

[51] A. Vahdati, S. Walscharts, I. Jonkers, J. Garcia-Aznar, J. Vander Sloten, G. van Lenthe, Role of subject-specific musculoskeletal loading on the prediction of bone density distribution in the proximal femur, J. Mech. Behav. Biomed. Mater. 30 (2014) 244–252 URL https://linkinghub.elsevier.com/retrieve/pii/S1751616113004037, doi:10.1016/j.jmbbm.2013.11.015.

[52] L. Geris, A. Gerisch, J.V. Sloten, R. Weiner, H.V. Oosterwyck, Angiogenesis in bone fracture healing: a bioregulatory model, J. Theor. Biol. 251 (1) (2008) 137–158, doi:10.1016/J.JTBI.2007.11.008.

[53] K. Mohaghegh, M.A. Pérez, J.M. García-Aznar, Accelerating numerical simulations of strain-adaptive bone remodeling predictions, Comput. Methods Appl. Mech. Eng. 273 (2014) 255–272, doi:10.1016/j.cma.2014.02.003.

[54] M. Berli, C. Borau, O. Decco, G. Adams, R.B. Cook, J.M. García Aznar, P. Zioupos, Localized tissue mineralization regulated by bone remodelling: a computational approach, PLoS One 12 (3) (2017) e0173228, doi:10.1371/journal.pone.0173228.

[55] J.Z. Bakdash, L.R. Marusich, Repeated measures correlation, Frontiers in Psychology 8 (2017), doi:10.3389/fpsyg.2017.00456.

[56] J. Currey, The many adaptations of bone, J. Biomech. 36 (10) (2003) 1487–1495, doi:10.1016/S0021-9290(03)00124-6.

[57] R.B. Martin, D.B. Burr, N.A. Sharkey, D.P. Fyhrie, Skeletal Tissue Mechanics, Springer New York, New York, NY, 2015, doi:10.1007/978-1-4939-3002-9.

[58] D. Chen, N. Bertollo, A. Lau, N. Taki, T. Nishino, H. Mishima, H. Kawamura, W.R. Walsh, Osseointegration of porous titanium implants with and without electrochemically deposited DCPD coating in an ovine model, J. Orthop. Surg. Res. 6 (1) (2011) 56, doi:10.1186/1749-799X-6-56.

[59] L. Bonewald, Use it or lose it to age: a review of bone and muscle communication, Bone 120 (2019) 212–218, doi:10.1016/j.bone.2018.11.002.

[60] M. Hackmann, T. Wizemann, S.H. Beachy (Eds.), Exploring Sources of Variability Related to the Clinical Translation of Regenerative Engineering Products, National Academies Press, Washington, D.C., 2019, doi:10.17226/25371.

[61] M. Viceconti, S. Olsen, L.-P. Nolte, K. Burton, Extracting clinically relevant data from finite element simulations, Clin. Biomech. 20 (5) (2005) 451–454, doi:10.1016/j.clinbiomech.2005.01.010.

[62] D.S. Elliott, K.J.H. Newman, D.P. Forward, D.M. Hahn, B. Ollivere, K. Kojima, R. Handley, N.D. Rossiter, J.J. Wixted, R.M. Smith, C.G. Moran, A unified theory of bone healing and nonunion, The Bone & Joint Journal 98–B (7) (2016) 884–891, doi:10.1302/0301-620X.98B7.36061.

[63] Y. Li, J. Zhou, P. Pavanram, M. Leeflang, L. Fockaert, B. Pouran, N. Tümer, K.-U. Schröder, J. Mol, H. Weinans, H. Jahr, A. Zadpoor, Additively manufactured biodegradable porous magnesium, Acta Biomater. 67 (2018) 378–392 URL https://linkinghub.elsevier.com/retrieve/pii/S174270611730764X, doi:10.1016/j.actbio.2017.12.008.

[64] C. Han, Y. Li, Q. Wang, S. Wen, Q. Wei, C. Yan, L. Hao, J. Liu, Y. Shi, Continuous functionally graded porous titanium scaffolds manufactured by selective laser melting for bone implants, J. Mech. Behav. Biomed. Mater. 80 (2018) 119–127 URL https://linkinghub.elsevier.com/retrieve/pii/S1751616118300171, doi:10.1016/j.jmbbm.2018.01.013.

[65] A.A. Zadpoor, H. Weinans, Patient-specific bone modeling and analysis: the role of integration and automation in clinical adoption, J. Biomech. 48 (5) (2015) 750–760, doi:10.1016/j.jbiomech.2014.12.018.

[66] A. Robling, C. Turner, Mechanotransduction in bone: genetic effects on mechanosensitivity in mice, Bone 31 (5) (2002) 562–569, doi:10.1016/S8756-3282(02)00871-2.

[67] I.J. Wallace, B. Demes, S. Judex, Ontogenetic and genetic influences on bone's responsiveness to mechanical signals, in: C.J. Percival, J.T. Richtsmeier (Eds.), Building Bones: Bone Formation and Development in Anthropology, Cambridge University Press, Cambridge, 2017, pp. 233–253, doi:10.1017/9781316388907.011.

[68] I.P. Geoghegan, D.A. Hoey, L.M. McNamara, Estrogen deficiency impairs integrin $\alpha v \beta 3$-mediated mechanosensation by osteocytes and alters osteoclastogenic paracrine signalling, Sci. Rep. 9 (1) (2019) 4654 URL http://www.nature.com/articles/s41598-019-41095-3, doi:10.1038/s41598-019-41095-3.

[69] I. Simfia, J. Schiavi, L.M. McNamara, ROCK-II inhibition suppresses impaired mechanobiological responses in early estrogen deficient osteoblasts, Exp. Cell Res. 396 (1) (2020) URL https://linkinghub.elsevier.com/retrieve/pii/S0014482720305139 112264, doi:10.1016/j.yexcr.2020.112264.

[70] A. Torcasio, X. Zhang, H. Van Oosterwyck, J. Duyck, G.H. van Lenthe, Use of micro-CT-based finite element analysis to accurately quantify peri-implant bone strains: a validation in rat tibiae, Biomech. Model. Mechanobiol. 11 (5) (2012) 743–750, doi:10.1007/s10237-011-0347-6.

[71] E. Schileo, F. Taddei, L. Cristofolini, M. Viceconti, Subject-specific finite element models implementing a maximum principal strain criterion are able to estimate failure risk and fracture location on human femurs tested in vitro, J. Biomech. 41 (2) (2008) 356–367, doi:10.1016/j.jbiomech.2007.09.009.

[72] J. Ganghoffer, R. Rahouadj, J. Boisse, J. Schiavi, A phase field approach for bone remodeling based on a second-gradient model, Mech. Res. Commun. 96 (2019) 37–44 URL https://linkinghub.elsevier.com/retrieve/pii/S0093641319300448, doi:10.1016/j.mechrescom.2019.02.007.

[73] K. Newell, J. Chitty, F.M. Henson, "Patient reported outcomes" following experimental surgery-using telemetry to assess movement in experimental ovine models, Journal of Orthopaedic Research 36 (5) (2018) 1498–1507, doi:10.1002/jor.23790.

[74] R.M. Wazen, J.A. Currey, H. Guo, J.B. Brunski, J.A. Helms, A. Nanci, Micromotion-induced strain fields influence early stages of repair at bone implant interfaces, Acta Biomater. 9 (5) (2013) 6663–6674 URL https://linkinghub.elsevier.com/retrieve/pii/S1742706113000202, doi:10.1016/j.actbio.2013.01.014.

[75] P. Moreo, M. Pérez, J. García-Aznar, M. Doblaré, Modelling the mechanical behaviour of living bony interfaces, Comput. Methods Appl. Mech. Eng. 196 (35–36) (2007) 3300–3314 URL https://www.sciencedirect.com/science/article/pii/S004578250700165X, doi:10.1016/J.CMA.2007.03.020.

[76] E.G. Meyer, C.T. Buckley, S.D. Thorpe, D.J. Kelly, Low oxygen tension is a more potent promoter of chondrogenic differentiation than dynamic compression, J. Biomech. 43 (13) (2010) 2516–2523 URL https://linkinghub.elsevier.com/retrieve/pii/S0021929010002939, doi:10.1016/j.jbiomech.2010.05.020.

[77] E. Borgiani, G.N. Duda, S. Checa, Multiscale modeling of bone healing: toward a systems biology approach, Frontiers in Physiology 8 (2017) URL http://journal.frontiersin.org/article/10.3389/fphys.2017.00287/full, doi:10.3389/fphys.2017.00287.

[78] A. Carlier, L. Geris, J. Lammens, H. Van Oosterwyck, Bringing computational models of bone regeneration to the clinic, Wiley Interdiscip. Rev. Syst. Biol. Med. 7 (4) (2015) 183–194, doi:10.1002/wsbm.1299.